Accepted for publication in *Applied Thermal Engineering* on September 29, 2014

CFD analysis of the impact of physical parameters on evaporative cooling by a mist spray system

Hamid Montazeri[1], Bert Blocken[1,2], Jan L.M. Hensen[1]

1 Building Physics and Services, Department of the Built Environment, Eindhoven University of Technology, P.O. box 513, 5600 MB Eindhoven, The Netherlands
2 Building Physics Section, Department of Civil Engineering, Leuven University, Kasteelpark Arenberg 40 – bus 2447, 3001 Heverlee, Belgium

Graphical abstract

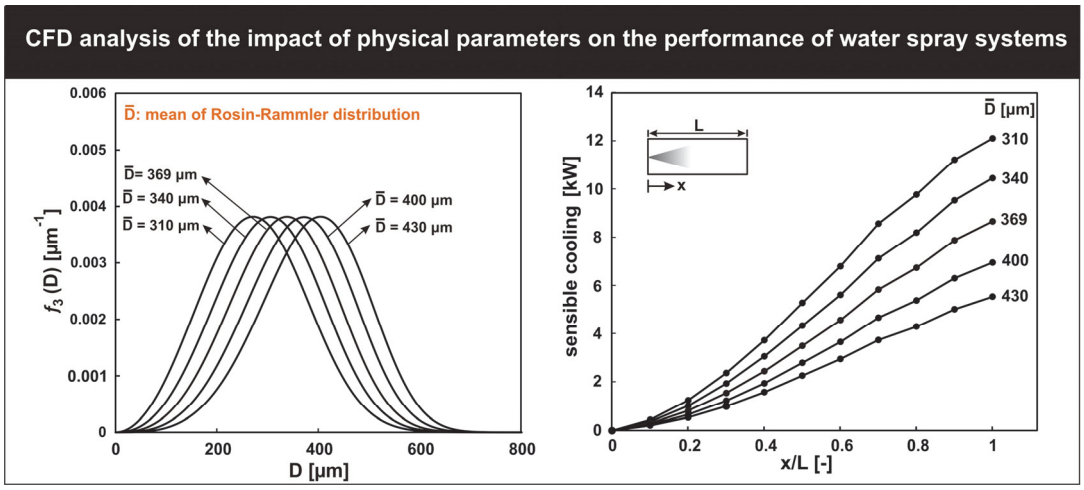

Research highlights:

- CFD simulation of evaporative cooling by water spray systems.
- Grid-sensitivity analysis and validation with wind-tunnel measurements.
- Analysis of the impact of physical parameters on the performance of the system.
- Injecting droplets with a temperature higher than DBT of air can provide cooling.
- The cooling performance of the system is enhanced for wider drop-size distributions.

CFD analysis of the impact of physical parameters on evaporative cooling by a mist spray system

Hamid Montazeri[*,1], Bert Blocken[1,2], Jan L.M. Hensen[1]

1 Building Physics and Services, Department of the Built Environment, Eindhoven University of Technology, P.O. box 513, 5600 MB Eindhoven, The Netherlands
2 Building Physics Section, Department of Civil Engineering, Leuven University, Kasteelpark Arenberg 40 – bus 2447, 3001 Heverlee, Belgium

Abstract: The evaporation of droplets in a turbulent two-phase flow is of importance in many engineering applications. Water droplet evaporation in spray systems, for example, is increasingly used in public spaces and near building surfaces to achieve immediate cooling and enhance the thermal comfort in indoor and outdoor environments. The complex two-phase flow in such a system is influenced by many parameters such as continuous phase velocity, temperature and relative humidity, drop size distribution, velocity and temperature of the droplets and continuous phase-droplet and droplet-droplet interactions. Most of these parameters are not easily varied independently. To gain insight into the performance of the system, however, detailed knowledge of the impact of every parameter is important. Computational Fluid Dynamics (CFD) is a useful tool for performing such parametric analyses. To the best of our knowledge, a detailed analysis of the cooling performance of a water spray system under different physical conditions has not yet been performed. This paper provides a systematic parametric analysis of the evaporative cooling provided by a water spray system with a hollow-cone nozzle configuration. The analysis is based on grid-sensitivity analysis and validation with wind-tunnel measurements. The impact of several physical parameters is investigated: inlet air temperature, inlet air humidity ratio, inlet air velocity, inlet water temperature and inlet droplet size distribution. The results show that for a given value of inlet water temperature (35.2 °C), as the temperature difference between the inlet air and the inlet water droplets increases from 0 °C to 8 °C, the sensible cooling capacity of the system improves by more than 40%. In addition, injecting water droplets with a temperature higher than the dry-bulb temperature of the air can still provide cooling, although the amount of cooling reduces considerably compared to the case with water at lower temperatures. It is also shown that as $\overline{D}$, the mean of the Rosin-Rammler distribution, is reduced from 430 to 310 μm, the cooling performance of the system is improved by more than 110%. For a given value of $\overline{D}$, the cooling is enhanced for wider drop-size distributions.

Keywords: Computational Fluid Dynamics (CFD), Validation, Parametric analysis, Hollow-cone spray, Water spray system

1 Introduction

The evaporation of spray droplets in a turbulent two-phase flow is important for many engineering applications, such as internal combustion engines, spray drying, fire suppression and evaporative cooling. Evaporative cooling by water spray systems, for example, is increasingly used to achieve immediate cooling and to enhance the thermal comfort in outdoor and indoor environments (e.g. [1–6]). Compared to other micro-climate control techniques, evaporative cooling introduces a number of advantages. It is an environmentally-friendly and cost-effective technique to improve the quality of indoor and outdoor environments because it makes use of passive cooling with relatively simple system components [7]. Evaporative cooling systems are unobtrusive which gives building designers and urban planners much flexibility for innovative system design concepts, and it allows easy integration in existing city infrastructures or renovation projects. The effect is controllable and can be employed in a dynamic way to operate only when cooling is desired. Most other climate change and/or urban heat island (UHI) mitigation/adaptation approaches, such as high-albedo surfaces, have an effect all year long, which implies they have a positive effect in warm seasons, but also negative side-effects such as increased energy consumption in winter [8,9].

* Corresponding author: Hamid Montazeri, Department of the Built Environment, Building Physics and Services, Eindhoven University of Technology, P.O. box 513, 5600 MB Eindhoven, the Netherlands. Tel: +31 (0)40 247 5790, Fax: +31 (0)40 243 8595. *E-mail address:* h.montazeri@tue.nl

In a water spray system, a cloud of very fine water droplets is produced using atomization nozzles. This enhances mixing and increases the contact surface area between the air and the water droplets resulting in a higher rate of evaporation, yielding greater cooling of the air. The complex two-phase flow in a water spray system is influenced by many physical parameters such as continuous phase velocity, temperature and relative humidity, drop size distribution, velocity and temperature of droplets and continuous phase-droplet and droplet-droplet interactions [10–13]. To gain insight into the performance of a water spray system, detailed knowledge of the impact of every aforementioned physical parameter is important.

Research on the cooling performance of water spray systems was mainly performed by full-scale measurements [15], wind-tunnel measurements [16] and Computational Fluid Dynamics (CFD) [13,17–19]. CFD is a useful tool for performing parametric studies for complex flows. This is especially the case for the two-phase flow in water sprays as the evaporation process depends on several physical parameters that are not easily varied independently. CFD also offers the advantage that the latent heat and sensible heat fluxes during the evaporation process can separately be determined. CFD is capable of providing whole-flow field data, i.e. data on the relevant parameters of the two phases in all points of the computational domain. In addition, it provides a high level of control over the boundary conditions. For this reason, CFD is increasingly used for basic and applied research in urban physics and environmental wind engineering, as demonstrated by several review papers [20–28]. Example applications for which CFD is frequently used are pollutant dispersion [21,27], natural ventilation of buildings and streets [29–36], wind-driven rain on buildings [20] and pedestrian-level wind comfort [22,37]. Although not in urban context, CFD has also been used on several occasions in the past to evaluate the performance of spray systems for different applications (e.g.[14,18,38–40]). In the vast majority of these studies, the Lagrangian-Eulerian (LE) approach has been used. This approach, which has several advantages over the Eulerian-Eulerian approach [41], is also used in the present paper. Detailed knowledge of the impact of both computational and physical parameters is important for the accuracy of CFD simulations and optimizing spray performance. Some previous studies already analyzed the impact of computational parameters for water spray systems [13,19]. For example, a systematic evaluation of the LE approach for predicting evaporative cooling provided by a water spray system was carried out by the present authors in Ref. [13]. Some previous studies also already analyzed the impact of physical parameters [12,18]. However, to the best of our knowledge, none of these studies included grid-sensitivity analysis, and none of them included a drop spectrum rather than a single drop size.

Therefore, this paper investigates the impact of physical parameters, including drop spectra, based on grid-sensitivity analysis and detailed validation with wind-tunnel experiments. It evaluates the evaporative cooling process provided by a water spray system with a hollow-cone nozzle configuration. The impact of the following physical parameters is investigated: inlet dry-bulb air temperature, inlet humidity ratio, inlet air velocity, inlet water temperature and inlet droplet size distribution.

In section 2, the wind-tunnel experiments by Sureshkumar et al. [16] that are used for the validation study are briefly outlined. Section 3 presents an overview of the computational settings and parameters for the reference case. The validation of the CFD results with the wind-tunnel measurements is also presented in this section. In section 4, the impact of the physical parameters is investigated. The limitations of the study are discussed in section 5. The main conclusions are presented in section 6.

2 Wind-tunnel measurements

The evaporative cooling performance of a hollow-cone nozzle spray system was investigated by Sureshkumar et al. [16] using wind-tunnel measurements. The experiments were performed in an open-circuit wind tunnel with a uniform approach-flow mean wind speed. The test section of the wind tunnel was 1.9 m long with a cross section of 0.585×0.585 m^2 (Fig. 1a). The inlet air dry-bulb temperature (DBT) and wet-bulb temperature (WBT) were measured by two thermocouples placed upstream of the spray nozzle. The exact position of the thermocouples was not provided by Sureshkumar et al. [16]. Note that only two thermocouples were used, but that the approach-flow is assumed to be of uniform characteristics due to upstream mixing in the wind-tunnel. The outlet DBT and WBT variations were measured with thermocouples at nine positions across the outlet plane of the test section (Fig. 1b).

Electric heaters were employed upstream of the tunnel blower to reduce the effect of the background air temperature fluctuations. These fluctuations were limited within ±0.3 °C during each set of experiments. A thermal probe installed upstream of the spray nozzle was used to measure the air stream velocity. The maximum experimental uncertainty for the mean velocity was estimated to be less than ±0.05 m/s for air velocity up to 2 m/s and ±0.2 m/s for air velocity between 2 and 4 m/s.

To avoid wetting of the thermocouples, the remaining water droplets in the air flow were collected by the use of a drift eliminator with z-shaped plates placed close to the tunnel outlet. The inlet and outlet

water temperatures were measured using two thermocouples upstream of the nozzle and downstream of the drift eliminator, respectively. Water pressure was also measured by a pressure gauge upstream of the nozzle.

Four identical nozzles but with different discharge openings of 3, 4, 5 and 5.5 mm were used to evaluate the impact of nozzle characteristics on cooling performance of the spray system. Each nozzle was installed in the middle of a cross-section of the test section (Fig. 1a) and designed in a way that the exiting water forms a hollow-cone sheet disintegrating into droplets. The droplet diameter distribution was determined using an image-analysing technique. The uncertainty of this technique for the mean droplet size was estimated to be ±22 %. The impact of the mean of the droplet size distribution will be investigated in subsection 4.5.1. The half-cone angle was measured in still air and reported as a function of discharge opening, water pressure and inlet air velocity. No correlations between droplet size and velocity were given by Sureshkumar et al. [16].

The experiments were conducted for 36 cases; four different nozzle discharge diameters (i.e. 3, 4, 5 and 5.5 mm), three inlet nozzle gauge pressures (1, 2 and 3 bar) and three inlet air velocity values (1, 2 and 3 m/s). In the present study, the case with nozzle discharge diameter of 4 mm, gauge pressure of 3 bar and inlet air speed of 3 m/s is withheld for the validation study since droplet size distribution data are also available for these cases. A list of some main parameters of the reference case is presented in Table 1.

3 CFD simulations: reference case

In this study the commercial CFD code ANSYS/Fluent 12.1 [42] is used in which the Lagrangian-Eulerian approach is implemented to simulate multi-phase flows in sprays and atomizers.

3.1 Computational geometry and grid

A computational model was made of the wind-tunnel test section with dimensions 0.585 × 0.585 × 1.9 m^3 (Fig. 2a). Geometry and grid generation was executed with the pre-processor Gambit 2.4.6, resulting in a grid with 1,018,725 hexahedral cells (Fig. 2b). The minimum and maximum cell volumes in the domain are approximately 1.9×10^{-8} m^3 and 5.9×10^{-6} m^3, respectively. The distance from the centre point of the wall adjacent cell to the walls is 0.006 m. This corresponds to y* values between 35 and 135 for the case with the maximum inlet air velocity (i.e. 3 m/s). As standard wall functions are used in this study, these values ensure that the centre point of the wall-adjacent cell is placed in the logarithmic region of the boundary layer. The grid resolution resulted from a grid-sensitivity analysis. More information about the grid can be found in Ref. [13].

3.2 Boundary conditions

In the simulations, the mean velocity inlet boundary condition for the continuous phase is a uniform profile according to the measured data (=U_∞). As the turbulence characteristics of the flow were not reported by Sureshkumar et al [16], a turbulence intensity, I, of 10% is assumed for the inlet flow, which is relevant for practical applications and for the atmospheric boundary layer wind flow. In addition, a sensitivity analysis done by the current authors (not shown in this paper) shows that the impact of the turbulence intensity (TI < 10%) on the results is negligible. The main reason for this could be related to the high inertia of droplets. The turbulent kinetic energy k is calculated from U_∞ and I using Eq. (1). The turbulence dissipation rate, ε, is given by Eq. (2) where C_μ is a constant (~ 0.09). The turbulence length scale, l, in this equation is taken as $l = 0.07D_H$ where D_H is the hydraulic diameter of the domain which is equal to the width of the test section (= 0.585 m).

$$k = (U_\infty . I)^2 \tag{1}$$

$$\varepsilon = C_\mu^{3/4} \frac{k^{3/2}}{l} \tag{2}$$

The thermal boundary condition at the inlet is a constant temperature equal to the measured inlet DBT. A fixed vapour mass fraction is also calculated based on the experimental data and imposed at the inlet as a boundary condition for the vapour transport equation. The vapour mass fraction for the moist air can be taken as x/(x+1) where x ($kg_{vapour}/kg_{dry\text{-}air}$) is the humidity ratio of air. The walls of the computational domain are modelled as no-slip walls with zero equivalent sand-grain roughness height $k_S = 0$ in the roughness modification of the wall functions [43]. The standard wall functions by Launder

and Spalding [44] are applied. The adiabatic thermal boundary condition is used for these surfaces. Zero static gauge pressure is applied at the outlet plane.

The "reflected" boundary condition is imposed to take the effect of the wind-tunnel walls on the impinging drops into account. Using this boundary condition, it is possible to define the amount of momentum in the directions normal and tangential to the wall that is retained by the particle after the collision with the boundary. In this study, it is assumed that after impingement the normal momentum component is zero while the tangential component remains the same. In this case, there will be a water film on the wall in the lower part of the domain. For the top of the domain, however, droplets rebound and move downward under influence of gravity. When droplets impinge on solid surfaces, different phenomena can occur, which depend on the physical properties of the droplets such as surface tension, viscosity, density, temperature and diameter, and on impingement conditions such as impact angle and velocity of droplets relative to the wall [45–48]. In addition, many studies investigated the influence of wall characteristics such as roughness, temperature and wettability of the surface (e.g. Ref. [49]). A detailed review of studies on droplet-wall impact can be found in Moreira et al. [50]. Depending on the mentioned conditions, droplets may float and be lost in a liquid film, may be reflected or may disintegrate into smaller droplets. As the temperature of the wall in the experiments by Sureshkumar et al. [16] is less than the boiling temperature and the Leidenfrost temperature of the droplets, for the simulations it is assumed that the droplets are entrained in a water film along the walls after impingement [47]. The presence of a liquid on the surface changes the boundary condition and the impact leads to a liquid–liquid interaction. In this case, the impact characteristics depend on the surface roughness but also the film thickness compared with the droplet size [51]. However, the effect of the film thickness is not taken into account.

As mentioned in section 2, in the experiments a drift eliminator was used near the outlet plane. In this study the drift eliminator is not included in the computational domain because a detailed description of its characteristics was not reported by Sureshkumar et al. [16]. However, the impact of such plates is taken into account by using the "escape" boundary condition at the outlet, assuming that the upstream impact of the drift eliminator on the air flow pattern is negligible. By using this boundary condition, droplets leave the domain with their current conditions (i.e. velocity, temperature and vapour mass fraction at the outlet plane) and trajectory calculations are terminated [42].

3.3 Droplet characteristics

In the experiments by Sureshkumar et al. [16], an image-analysing technique was employed to determine the droplet size distribution. The Rosin-Rammler [52] model is used to describe the size distribution of the droplets in the CFD simulations. This model assumes an exponential relationship between the droplet diameter, D, and the mass fraction of droplets with diameters greater than D, which can be expressed as [53]:

$$Y_D = e^{-\left(D/\overline{D}\right)^n} \tag{3}$$

where Y_D is the mass fraction of droplets with diameters greater than D, $\overline{D}$ the mean drop diameter and n the spread parameter as an indicator of the distribution width. For the current experimental data, $\overline{D}$ and n are 369 µm and 3.67, respectively [13]. The experimental data and the Rosin-Rammler curve fit are shown in Fig. 3a. The Rosin-Rammler volume density distribution of the droplets can be calculated as follows [54,55]:

$$f_3(D) = \frac{n}{\overline{D}}\left(\frac{D}{\overline{D}}\right)^{n-1} e^{-\left(D/\overline{D}\right)^n} \tag{4}$$

Fig. 3b shows the results according to Eq. 4. The total number of droplet (particle) streams in the CFD simulations is assumed to be 300 meaning that they are released from 300 uniformly-distributed points on the nozzle opening perimeter. This number is taken based on the results of a sensitivity analysis provided in Ref [13] by the same authors. The results of this analysis show that approximately 300 streams are needed to obtain CFD result that are nearly independent of the number of droplet streams. In this case, using a larger number of streams would increase the computational time without any considerable effect on the accuracy of CFD results. Using a lower number of streams, however, would lead to a high discrepancy between the CFD results and experimental data. In this study, the smallest droplet diameter to be considered in the size distribution of the Rosin-Rammler model is 74 µm, corresponding to the minimum resolution of the droplet measurements. The largest droplet diameter is considered 518 µm, based on the largest droplet diameter in the samples [16]. 20 discrete droplet

diameters, N_D, are assumed to be injected from each droplet stream into the domain. The droplet diameters are distributed at equally spaced intervals of $(D_{max}-D_{min})/N_D$.

The spherical drag law is used to estimate the drag coefficients acting on the droplets. Various correlations for the drag coefficient of spherical droplets (particles) can be found in the literature (e.g.[56–58]). In the present study the correlation by Morsi and Alexander [59] is used.
This correlation proposes the following drag coefficients for a wide range of Reynolds numbers up to 5 $\times 10^4$:

$$C_d = \frac{K_1}{Re} + \frac{K_2}{Re^2} + K_3 \quad (5)$$

In which K_1, K_2 and K_3 are constants (Table 2).

The flux of droplet vapour into the air, N (kgmol/m^{2}s), is calculated using the gradient of the vapor concentration between the droplet surface and the air (Eq. 6):

$$N = k_c\left(C_{i,s} - C_{i,\infty}\right) \quad (6)$$

where k_c is the mass transfer coefficient (m/s), $C_{i,s}$ the vapor concentration at the droplet surface (kgmol/m^3) and $C_{i,\infty}$ the vapor concentration in the bulk gas (kgmol/m^3). The mass transfer coefficient is taken from the Sherwood number correlation [59]:

$$Sh = \frac{k_c d_p}{D_{i,m}} = 2.0 + 0.6 Re_d^{0.5} Sc^{0.33} \quad (7)$$

where d_p is the droplet diameter (m), $D_{i,m}$ diffusion coefficient of vapour in the air (m^2/s), Re_d the Reynolds number based on the droplet diameter and the relative velocity. Sc is the Schmidt number ($\mu/\rho D_{m,i}$). Note that the mass of the droplet, in each time step Δt (sec.), is reduced with a rate of $NA_pM_w\Delta t$ in which A_p is surface area of the droplet (m^2), M_w the molecular weight of water. Eq. (7) expresses the relationship between mass transfer coefficient and droplet diameter, which can be rewritten as:

$$k_c = \frac{D_{i,m}}{d_p}\left(2.0 + 0.6\left(\frac{u d_p}{\vartheta}\right)^{0.5} Sc^{0.33}\right) \quad (8)$$

In the simulations, shrinkage of the droplets is taken into account. Note that, as the drop diameter reduces, the transfer coefficient k_c increases. The spray is assumed to be dilute and collision of droplets is not taken into account.

3.4 Spray nozzle characteristics

The water droplets are injected into the computational domain from a nozzle with 4 mm diameter positioned in the middle of the inlet plane of the computational domain and oriented horizontally in downstream direction. The total mass flow rate and temperature of the injected water droplets are imposed according to the experimental data (Table 1). The hollow cone spray model provided by Ansys/Fluent 12.1 [42] is used. In this model, the sheet velocity, U_0, is used for the initial velocity of the droplet streams. U_0 is calculated as $C_v\,(2\Delta P/\rho_w)^{0.5}$ where C_v is the nozzle coefficient, ΔP the pressure difference along the nozzle and supply pipe and ρ_w the water density. As recommended by Sureshkumar et al. [17], for the given nozzle C_v is approximately 0.9.

3.5 Solver settings

The continuous phase and discrete phase flows are solved in a fully coupled manner. Concerning the discrete phase, the droplet momentum, heat and mass transfer equations are solved in a fully coupled manner.

For the continuous phase flow, the 3D steady RANS equations for conservation of mass, momentum and energy are solved in combination with the realizable k-ε turbulence model by Shih et al. [60]. The analysis of the sensitivity of the results to the turbulence model by Montazeri et al. [13] showed that none of the investigated turbulence models was superior over the others. The SIMPLE algorithm is used for pressure-velocity coupling, pressure interpolation is second order and second-order discretisation schemes are used for both the convection terms and the viscous terms of the equations.

Lagrangian trajectory simulations are performed for the discrete phase. The discrete phase interacts with the continuous phase, and the discrete phase model source terms are updated after each continuous phase iteration. To solve the equations of motion for the droplets, the Automated Tracking Scheme Selection is adopted to be able to switch between higher order lower order tracking schemes. This

mechanism can improve the accuracy and stability of the simulations [42]. In this study, trapezoidal and implicit schemes are used for higher and lower order schemes, respectively.

3.6 CFD results and comparison with wind-tunnel experiments

Fig. 4 presents a comparison between the CFD results for the reference case, shown in Table 1, and the wind-tunnel experiments [16]. The comparison is performed for the DBT, WBT and specific enthalpy values at the nine measurement points. The specific enthalpy of moist air, h, can be expressed as $h = h_{dry.air} + x \, . \, h_v$, where $h_{dry.air}$ is the specific enthalpy of dry air (kJ/ $kg_{dry.air}$) given by $C_p.T$, where C_p is the specific heat capacity of air (kJ/$kg_{dry.air}$.K) and T the dry-bulb air temperature (K). x is the humidity ratio ($kg_{vapour}/kg_{dry.air}$) and h_v the specific enthalpy of water vapour. Note that h_v can be expressed as $C_{pv}.T + h_{evaporation}$ in which C_{pv} is the specific heat capacity of air (kJ/kg.K) and $h_{evaporation}$ is the evaporation heat of water (kJ/kg). The results in Fig. 4 show a good agreement, within 10% for DBT, 5% for WBT and 7% for h. As pointed out by Montazeri et al. [13], the exact reasons for these deviations are not clear, but they are probably caused by a combination of limitations of the LE approach and experimental uncertainties. Apart from the LE approach limitations, the impact of collision of droplets, droplets impingement on solid surfaces and the drift eliminator on the airflow are not considered in this study. For the experimental uncertainties, as mentioned by Sureshkumar et al. [16], the dominant uncertainty of the experiments is for the WBT measurements. Other experimental uncertainties might be related to the technique used to determine the droplet size distribution. More information on the results and sensitivity of the results to the computational parameters can be found in Ref. [13].

4 CFD simulations: parametric analysis for physical parameters

The parametric analysis is performed for various physical parameters by applying systematic changes to the reference case (Table 1). In every subsection below, one of the parameters is varied, while all others are kept the same as in the reference case. Some main parameters of the cases that are investigated are given in Table 3. For each case, the downstream variation of the air temperature and humidity ratio averaged over vertical cross-sections are investigated. The change in sensible heat of the moist air along the domain is also analysed as an indication of the cooling capacity of the spray system. Note that the sensible heat of moist air is calculated as $C_p.T + x.C_{pv}.T$. In the remainder of this paper, we will refer to this change as sensible cooling of the spray system.

The impact of evaporative cooling by a water spray system on human comfort depends on the complex interplay between different climatic variables [61] and spray characteristics. To gain insight into the capability of the spray system to enhance thermal comfort, the Universal Thermal Climate Index (UTCI) [62,63] is also calculated along the domain. UTCI is a thermal comfort indicator for outdoor and semi-enclosed environments. It is an equivalent temperature, derived based on the Fiala multi-node model [64,65], which reflects the human physiological reaction to meteorological parameters including air temperature and humidity, wind speed and mean radiant temperature [66]. In this study, the mean radiant temperature is assumed constant $T_{mrt} = 35$ ℃ for all cases, while the other parameters are obtained from the CFD simulations. The UTCI is used here because in urban areas, water spray systems are generally applied in outdoor or semi-enclosed environments. Note however that the computational domain in the present study is kept equal to the wind-tunnel test section.

4.1 Impact of inlet dry-bulb air temperature

Fig. 5 shows the impact of the inlet dry-bulb air temperature on the performance of the spray system along the domain. The evaluation is for five temperature differences between the inlet air and the water droplets, $\Delta T_{a\text{-}d,\,inlet} = T_{air,inlet} - T_{droplet,inlet}$. The inlet water temperature is identical for all cases, i.e. $T_{droplet,inlet}$ = 35.2 °C. $\Delta T_{a\text{-}d,inlet}$ ranges from 8 °C to -8 °C. In the last case, for example, the temperature of the water droplets is 8°C higher than that of the inlet air. It can be seen that for the highest value of $\Delta T_{a\text{-}d,inlet}$, the largest overall air temperature reduction, i.e. the difference between the inlet and outlet, is achieved (9.3 °C) (Fig. 5a). The overall air temperature reduction declines monotonically by reducing $\Delta T_{a\text{-}d,inlet}$. For example, when $\Delta T_{a\text{-}d,inlet}$ = -8 °C the reduction is about 3.3 °C. Note that for this case, the air temperature increases until about half the length of the domain because of the dominant effect of convective heat transfer from the droplets, which have a higher temperature relative to the air.

Fig. 5b presents the change in the humidity ratio along the domain. The change is approximately independent of the inlet air temperature. At the outlet plane, the change in the humidity ratio reduces by less than 3% as $\Delta T_{a\text{-}d,inlet}$ is decreased from 8 to -8 °C.

The variation in the air sensible cooling along the domain relative to the inlet value is presented in Fig. 5c. The spray system provides 9.8 kW sensible cooling for the largest $\Delta T_{a\text{-}d,inlet}$. By reducing $\Delta T_{a\text{-}}$

$_{d,inlet}$, the cooling is also reduced monotonically and reaches about 4.1 kW for the case $\Delta T_{a\text{-}d,inlet}$ = -8 °C, which is still substantial. The performance of the spray system in providing a reduction of the UTCI is shown in Fig. 5d. The results are consistent with the amount of sensible cooling presented in Fig. 5c.

For each case, the moist air conditions for the same cross sections along the domain are presented in the psychrometric chart in Fig. 6. It can be seen that because of the cooling and humidification process of the spray system, the dry-bulb temperature of the air reduces, while its wet-bulb temperature increases. In addition, the sensible heat of the air reduces, while its latent heat increases resulting in the overall increase in the enthalpy of the air. For example, for the case $\Delta T_{a\text{-}d,\ inlet}$ = -8 °C the sensible heat reduces by about 3.2 kJ/$kg_{dry\text{-}air}$, while the latent heat increment is about 14.1 kJ/$kg_{dry\text{-}air}$ (Fig. 6). In this case, the overall increase in the enthalpy of the air is about 10.9 kJ/$kg_{dry\text{-}air}$.

A closer look at Fig. 6 reveals that by increasing $\Delta T_{a\text{-}d,inlet}$ from -8 °C to 8 °C, the overall sensible heat between the outlet and inlet increases by about 184%, while the latent heat increment is about 3%.

The cooling efficiency (CE) of the system can be evaluated according to the data provided on the psychrometric chart. According to the ASHRAE handbook [67], the cooling efficiency is defined as the ratio of the dry-bulb temperature difference between the outlet and inlet of the wind-tunnel test-section, over the web-bulb depression. The web-bulb depression is the difference between the inlet dry-bulb temperature and inlet wet-bulb temperature [67]. As $\Delta T_{a\text{-}d,inlet}$ increases from -8 to 8 °C, the cooling efficiency is increased from about 25% to more than 40%.

4.2 Impact of inlet air humidity ratio ω

Fig. 7 presents the impact of the inlet air humidity ratio ω of the air on the cooling performance of the system. The evaluation is carried out for five values of ω = 0.0026, 0.0052, 0.0078, 0.0104 and 0.0130 $kg_{vapour}/kg_{dry\text{-}air}$ corresponding to relative humidities 5.9, 11.8, 17.6, 22.4 and 29.1%, respectively. Note that the inlet air and inlet water temperatures are identical for all cases and equal to 39.2 and 35.2 °C. It can be seen that, as expected, the highest overall air temperature reduction (Fig. 7a), sensible cooling (Fig. 7c) and UTCI reduction (Fig. 7d) along the domain correspond to the case with the lowest amount of vapour in the inlet air. For low values of the inlet air humidity ratio the gradient of the vapour concentration between the droplet surface and the air increases leading to a higher rate of evaporation and higher change in the value of the air humidity ratio along the domain.

The moist air conditions for all cases in the psychrometric chart are shown in Fig. 8. It can be seen that by increasing the inlet humidity ratio, the process line tends to track the constant enthalpy line and the increase in the wet-bulb temperature of the air is negligible (about 1%). In this case, the cooling efficiency (CE) decreases from about 37% for ω = 0.0026 to less than 21% for ω = 0.0130.

4.3 Impact of inlet air velocity

The impact of the inlet air velocity on the performance of the system is shown in Fig. 9 for five velocity differences between the inlet water droplets and the air, $\Delta U_{d\text{-}a,inlet} = U_{droplet,inlet} - U_{air,inlet}$ = 7, 10, 13, 16 and 19 m/s. The inlet velocity of the droplets is $U_{droplet,inlet}$ = 22 m/s for all cases. The largest overall air temperature reduction (Fig. 9a) and air humidity ratio increase (Fig. 9b) are achieved for the highest value of $\Delta U_{d\text{-}a,inlet}$ (i.e. 19 m/s). By increasing the velocity difference from 7 to 19 m/s (i.e. reducing the inlet air velocity), the overall temperature reduction in the entire domain increases by 89%. In this case, the cooling efficiency (CE) of the system increases from about 3%, for $\Delta U_{d\text{-}a,inlet}$ = 7 m/s, to more than 35% for the highest velocity difference. The main reason is that a rise in the relative velocity of the two phases increases the heat and mass transfer coefficients of the droplets. In addition, the larger $\Delta U_{d\text{-}a,inlet}$ and therefore the lower $U_{air,inlet}$ leads to an increase in the residence time of droplets within the domain, resulting in a larger droplet interaction time with the surrounding air, more time for evaporation and a higher outlet DBT and humidity ratio.

As pointed out by Sommerfeld and Qiu [68], a reduction in the inlet air velocity allows a larger radial spread of the droplets in the spray. However, for the range of the relative velocities studied in this paper ($\Delta U_{d\text{-}a,inlet}$ = 7- 19 m/s) such a spread cannot be observed, especially close to the nozzle. Fig. 10 shows the temperature distributions in the vertical centre plane for the two cases $\Delta U_{d\text{-}a,inlet}$ = 7 and 19 m/s. It can be seen that for $\Delta U_{d\text{-}a,inlet}$ = 7 m/s the air can compress the spray further away from the nozzle, where the momentum of the droplets is reduced.

4.4 Impact of inlet water temperature

The impact of the inlet water temperature is investigated for five values of $\Delta T_{a\text{-}d,inlet} = T_{air,inlet} - T_{droplet,inlet}$. For comparison purposes, the same range of $\Delta T_{a\text{-}d,inlet}$ presented in subsection 4.1 is used, i.e. $\Delta T_{a\text{-}d,inlet}$ =

-8, -4, 0, 4 and 8 °C. The inlet air temperature is 39.2 °C for all cases. The results are shown in Fig. 11. It can be seen that by decreasing the water temperature by more than 33%, the sensible cooling is increased by more than 180%.

Table 4 compares the sensible cooling provided by the system for different values of the inlet air temperature, at a constant water temperature (Fig. 5), and the inlet water air temperature, at a constant inlet air temperature (Fig. 11). It shows that for a same value of $\Delta T_{a\text{-}d,inlet}$, lower values of the inlet air dry-bulb temperature and inlet water temperature improve the cooling performance of the system to a similar extent. However, as can be seen from comparing the columns in Table 4, combinations of inlet air DBT and inlet water temperature with lower absolute values of these temperatures yield a slightly higher sensible cooling than combination with higher absolute values.

4.5 Impact of droplet size distribution

In this part, the impact of droplet size distribution on the cooling performance of the system is presented. The evaluation is carried out in two parts: first for different values of $\overline{D}$, the mean of the Rosin-Rammler distribution and second for different values of n, the spread parameter of the distribution. In this section, the smallest and largest droplet diameters to be considered in the size distribution of the Rosin-Rammler model are 10 and 800 μm, respectively.

4.5.1 Impact of the mean of the distribution ($\overline{D}$)

In order to investigate the impact of the size of the droplets on the performance of the system, five droplet distributions corresponding to different values of $\overline{D}$ are imposed. To perform an appropriate comparison, all droplets in each distribution experience the same size enlargement/reduction as the one for $\overline{D}$, meaning that the whole Rosin-Rammler distribution in Fig. 3b is shifted along the x-axis. In this case, for each distribution the mass fraction of droplets with diameter $\Delta + D$ is the same as the one for the reference case with diameter D, i.e. $Y_D = Y_{D+\Delta}$, where Δ is the droplet size enlargement/reduction of $\overline{D}$. It gives $\lfloor D/\overline{D} \rfloor^{n_{ref}} = \lfloor (D+\Delta)/(\overline{D}+\Delta) \rfloor^{n_i}$ (Eq. 4) in which n_{ref} is the spread parameter of the reference case, i.e. 3.67. n_i, the spread parameter of each distribution, can be calculated by averaging over the entire range of droplet diameters. The results are shown in Fig. 12. In this study, five values of $\overline{D}$ are used: 310, 340, 369, 400 and 430 μm. The corresponding n values are 3.02, 3.35, 3.67, 4.00 and 4.33, respectively.

The profiles of the average air temperature and the change in the humidity ratio, sensible cooling and UTCI along the domain for different values of $\overline{D}$ are shown in Fig. 13. As the water flow rate is constant for all cases, a reduction in $\overline{D}$ increases the effective surface area of the droplets, resulting in a higher rate of heat and mass transfer from the droplets. For example, as $\overline{D}$ reduces from 430 to 310 μm (~28% reduction), the overall air temperature reduction from the inlet to outlet and the change in the humidity ratio along the domain increase by more than 16% and 88%, respectively. In addition, the sensible cooling of the system rises from 5.5 kW to 12.1 kW. Consequently, the UTCI reduction along the domain increases from 3.7 °C for $\overline{D} = 430$ μm to 8.7 °C for $\overline{D} = 310$ μm (Fig. 12d).

4.5.2 Impact of the spread parameter of the distribution (n)

In this section, five distributions corresponding to five values of n, ranging from 3.3 to 4.9, are considered. $\overline{D}$, is identical (369 μm) for all cases. The volume density distributions of the droplets are shown in Fig. 14. It can be seen that the width of the distribution decreases as the spread parameter, n, increases. The higher the value of n, the more uniform the droplet size distribution is in the spray.

Fig. 15 indicates the profiles of the average air temperature, humidity ratio, sensible cooling and UTCI variation along the domain. For a constant value of $\overline{D}$, the spray system shows a better performance for lower values of n, i.e. wider distribution.

Fig. 16a shows the normalized mass flow rate of evaporated droplets in the domain for different values of n. It can be seen that this amount decreases by increasing n. This reduction is consistent with the amount of moisture absorbed by the air presented in Fig. 15b. Note that widening the distribution leads to an increase in the number of small and large droplets simultaneously. Fig. 16b shows the proportion of the mass flow rate of the evaporated droplets for two droplet size groups: droplets with the size diameters larger than $\overline{D} = 369$ μm and smaller than this value. For all values of n, the mass flow rate of the small droplets ($D < \overline{D}$) is considerably higher than the one for the large droplets ($D > \overline{D}$). For the case with n = 3.3, for example, this ratio is about 5.3. In addition, by decreasing n from 4.9 to 3.3, the evaporation rate of the small droplets increases by more than 8.3% showing the importance of small droplets in a droplet size distribution.

5 Discussion

This study presents a detailed and systematic parametric analysis to investigate the impact of different physical parameters on the cooling performance of a water spray system with a hollow-cone nozzle configuration. The Lagrangian-Eulerian (3D steady RANS) approach was used. Some important limitations of this study need to be mentioned:

1) This study focuses on the immediate cooling that is achieved close by the nozzle of a water spray system. More simulations need to be performed to investigate the cooling performance of the system further downstream of the nozzle. It is also important to investigate whether complete evaporation takes place in a large-scale domain. This is relevant for application in urban areas, where not only the cooling effect, but also the wetting of people should be considered.
2) In this study, droplets are injected into the domain parallel to the inlet flow. The cooling performance of similar systems in cross-flow conditions needs to be investigated.
3) In this study, the performance of a spray system with a uniform inlet air velocity is investigated. Further studies need to be carried out to evaluate the performance of the system immersed in an atmospheric boundary layer.

This study is intended to evaluate the potential of water spray systems in mitigating the heat stress in the outdoor environment for different spray characteristics and air flow conditions. The results contain useful information that can be used as design guidance for evaporative cooling system engineers and designers.

The results of this study show that using small droplets with a wide size distribution can improve the cooling performance of such a system. It can also lead to complete evaporation of the droplets, which is desired in public spaces to avoid the wetting of people. In addition, injecting the droplets at a higher velocity and lower temperature relative to the ambient air will increase the performance of the system. Note that spray characteristics such as water temperature, water flow rate, droplet size and droplet distribution can be adjusted during operation in response to local climate conditions. On the other hand, meteorological parameters such as air velocity and air temperature are of course not controllable. The relationships presented in this paper can be helpful to devise appropriate control strategies that will help to ensure maximum system performance under varying meteorological conditions, such as air temperature, air humidity and air velocity.

6 Conclusion

This paper provides a systematic parametric analysis to evaluate the evaporative cooling process provided by a water spray system with a hollow-cone nozzle configuration. The evaluation is based on grid-sensitivity analysis and validation with wind-tunnel measurements. The impact of several physical parameters is investigated: inlet air temperature, inlet air humidity ratio, inlet air velocity, inlet water temperature and droplet size distribution. Within the range of the parameters studied, the following conclusions can be drawn:

1) The inlet dry-bulb air temperature has a strong effect on the amount of sensible cooling providing by a water spray system. The results show that:
   - For a given value of the inlet water temperature (35.2 °C), as the temperature difference between the inlet air and the inlet water droplets increases from 0 °C to 8 °C, the sensible cooling capacity of the system improves by more than 40%.
   - Injecting warmer water relative to the inlet air can still provide cooling, though the amount of cooling reduces considerably compared to the case with a colder water. In this case, the immediate cooling (close by the nozzle) cannot be achieved.
   - The impact of the inlet air temperature on the air humidity ratio is not significant. At the outlet plane, the change in the humidity ratio reduces by less than 3% as $\Delta T_{a\text{-}d,inlet}$ is decreased from 8 to -8 °C.
2) The moisture content of the inlet air (inlet humidity ratio) influences the rate of evaporation. A lower amount of moisture in the air improves the performance of the spray system. In this case, the cooling efficiency (CE) increases from about 21% for $\omega = 0.0130$ to 37% for $\omega = 0.0026$.
3) A lower value of the inlet air velocity relative to the droplets (higher velocity difference) improves the cooling performance of the system. For the considered inlet air velocities, 3 to 15 m/s, the change in the radial spread of the droplets in the spray is negligible, especially close to the nozzle.
4) For a constant value of the inlet dry-bulb air temperature, reducing the inlet water temperature improves the performance of the system.
5) Droplet size distribution is an important parameter that influences the evaporation process of a spray system. The results show that:

- As $\overline{D}$, the mean of the Rosin-Rammler distribution, is reduced from 430 to 310 μm, the cooling performance of the system is improved by more than 110%.
- For a constant value of $\overline{D}$, the spray system shows a better performance for lower values of n, i.e. wider distribution.

Acknowledgements

This research was supported by the Dutch Knowledge for Climate Research Program within the theme Climate Proof Cities (CPC).

References

[1] Nishimura N, Nomura T, Iyota H, Kimoto S. Novel water facilities for creation of comfortable urban micrometeorology. Sol Energy 1998;64:197–207.
[2] Takahashi R, Asakura A, Koike K, Himeno S, Fujita S. Using snow melting pipes to verify water sprinkling's effect over a wide area. Sustain Tech Strateg Urban Water Manag 2010.
[3] Naticchia B, D'Orazio M, Carbonari A, Persico I. Energy performance evaluation of a novel evaporative cooling technique. Energy Build 2010;42:1926–38.
[4] Wong NH, Chong AZ. Performance evaluation of misting fans in hot and humid climate. Build Environ 2010;45:2666–78.
[5] Calautit JK, Chaudhry HN, Hughes BR, Ghani SA. Comparison between evaporative cooling and a heat pipe assisted thermal loop for a commercial wind tower in hot and dry climatic conditions. Appl Energy 2013;101:740–55.
[6] Wei J, He J. Numerical simulation for analyzing the thermal improving effect of evaporative cooling urban surfaces on the urban built environment. Appl Therm Eng 2013;51:144–54.
[7] Pearlmutter D, Erell E, Etzion Y, Meir IA, Di H. Refining the use of evaporation in an experimental down-draft cool tower. Energy Build 1996;23:191–7.
[8] Loonen R, Trčka M, Cóstola D, Hensen JLM. Climate adaptive building shells: State-of-the-art and future challenges. Renew Sustain Energy Rev 2013;25:483–93.
[9] Taleghani M, Tenpierik M, van den Dobbelsteen A. Energy performance and thermal comfort of courtyard/atrium dwellings in the Netherlands in the light of climate change. Renew Energy 2014;63:486–97.
[10] Lefebvre AH. Properties of sprays. Part Part Syst Charact 1989;6:176–86.
[11] Hou Y, Tao Y, Huai X, Guo Z. Numerical characterization of multi-nozzle spray cooling. Appl Therm Eng 2012;39:163–70.
[12] Alkhedhair A, Gurgenci H, Jahn I, Guan Z, He S. Numerical simulation of water spray for pre-cooling of inlet air in natural draft dry cooling towers. Appl Therm Eng 2013;61:416–24.
[13] Montazeri H, Blocken B, Hensen JLM. Evaporative cooling by water spray systems: CFD simulation, experimental validation and sensitivity analysis. Build Environ 2014. doi:10.1016/j.buildenv.2014.03.022.
[14] Ahmadikia H, Moradi A, Hojjati M. Performance Analysis of a Wind-Catcher With Water Spray. Int J Green Energy 2012;9:160–73.
[15] Belarbi R, Ghiaus C, Allard F. Modeling of water spray evaporation: Application to passive cooling of buildings. Sol Energy 2006;80:1540–52.
[16] Sureshkumar R, Kale SR, Dhar PL. Heat and mass transfer processes between a water spray and ambient air–I. Experimental data. Appl Therm Eng 2008;28:349–60.
[17] Sureshkumar R, Kale SR, Dhar PL. Heat and mass transfer processes between a water spray and ambient air–II. Simulations. Appl Therm Eng 2008;28:361–71.
[18] Kang D, Strand RK. Modeling of simultaneous heat and mass transfer within passive down-draft evaporative cooling (PDEC) towers with spray in FLUENT. Energy Build 2013;62:196–209. doi:10.1016/j.enbuild.2013.02.039.
[19] Li X, Zbiciński I. A sensitivity study on CFD modeling of cocurrent spray-drying process. Dry Technol 2005;23:1681–91.
[20] Blocken B, Carmeliet J. A review of wind-driven rain research in building science. J Wind Eng Ind Aerodyn 2004;92:1079–130.
[21] Meroney RN. Wind tunnel and numerical simulation of pollution dispersion: a hybrid approach. Croucher Adv Study Inst Hong Kong Univ Sci Technol 2004:6–10.
[22] Mochida A, Lun IY. Prediction of wind environment and thermal comfort at pedestrian level in urban area. J Wind Eng Ind Aerodyn 2008;96:1498–527.
[23] Chen Q. Ventilation performance prediction for buildings: A method overview and recent applications. Build Environ 2009;44:848–58.

[24] Blocken B, Stathopoulos T, Carmeliet J, Hensen JL. Application of computational fluid dynamics in building performance simulation for the outdoor environment: an overview. J Build Perform Simul 2011;4:157–84.
[25] Ramponi R, Blocken B. CFD simulation of cross-ventilation for a generic isolated building: impact of computational parameters. Build Environ 2012;53:34–48.
[26] Moonen P, Defraeye T, Dorer V, Blocken B, Carmeliet J. Urban Physics: effect of the micro-climate on comfort, health and energy demand. Front Archit Res 2012;1:197–228.
[27] Tominaga Y, Stathopoulos T. CFD simulation of near-field pollutant dispersion in the urban environment: A review of current modeling techniques. Atmos Environ 2013;79:716–30.
[28] Blocken B. 50 years of Computational Wind Engineering: Past, present and future. J Wind Eng Ind Aerodyn 2014;129:69–102.
[29] Montazeri H, Azizian R. Experimental study on natural ventilation performance of a two-sided wind catcher. Proc Inst Mech Eng Part J Power Energy 2009;223:387–400.
[30] Montazeri H, Montazeri F, Azizian R, Mostafavi S. Two-sided wind catcher performance evaluation using experimental, numerical and analytical modeling. Renew Energy 2010;35:1424–35.
[31] Hooff T van, Blocken B. On the effect of wind direction and urban surroundings on natural ventilation of a large semi-enclosed stadium. Comput Fluids 2010;39:1146–55.
[32] Montazeri H. Experimental and numerical study on natural ventilation performance of various multi-opening wind catchers. Build Environ 2011;46:370–8.
[33] Ramponi R, Blocken B. CFD simulation of cross-ventilation for a generic isolated building: impact of computational parameters. Build Environ 2012;53:34–48.
[34] Blocken B, Gualtieri C. Ten iterative steps for model development and evaluation applied to Computational Fluid Dynamics for Environmental Fluid Mechanics. Environ Model Softw 2012;33:1–22.
[35] Montazeri H, Blocken B. CFD simulation of wind-induced pressure coefficients on buildings with and without balconies: validation and sensitivity analysis. Build Environ 2013;60:137–49.
[36] Allegrini J, Dorer V, Carmeliet J. Buoyant flows in street canyons: Validation of CFD simulations with wind tunnel measurements. Build Environ 2014;72:63–74.
[37] Montazeri H, Blocken B, Janssen WD, van Hooff T. CFD evaluation of new second-skin facade concept for wind comfort on building balconies: Case study for the Park Tower in Antwerp. Build Environ 2013;68:179–92.
[38] Dodge LG, Schwalb JA. Fuel spray evolution; Comparison of experiment and CFD simulation of nonevaporating spray. J Eng Gas Turbines PowerUSA 1989;111.
[39] Hua J, Kumar K, Khoo BC, Xue H. A numerical study of the interaction of water spray with a fire plume. Fire Saf J 2002;37:631–57.
[40] Wehrfritz A, Vuorinen V, Kaario O, Larmi M. Large Eddy Simulation of High-Velocity Fuel Sprays: Studying Mesh Resolution and Breakup Model Effects for Spray A. At Sprays 2013;23.
[41] Subramaniam S. Lagrangian–Eulerian methods for multiphase flows. Prog Energy Combust Sci 2013;39:215–45.
[42] ANSYS Inc. ANSYS Fluent 12.0 Theory Guide. USA: Lebanon 2009.
[43] Blocken B, Stathopoulos T, Carmeliet J. CFD simulation of the atmospheric boundary layer: wall function problems. Atmos Environ 2007;41:238–52.
[44] Launder BE, Spalding DB. The numerical computation of turbulent flows. Comput Methods Appl Mech Eng 1974;3:269–89.
[45] Frohn A, Roth N. Dynamics of droplets. Berlin: Springer; 2000.
[46] Karl A, Anders K, Rieber M, Frohn A. Deformation of liquid droplets during collisions with hot walls: experimental and numerical results. Part Part Syst Charact 1996;13:186–91.
[47] Anders K, Roth N, Frohn A. The velocity change of ethanol droplets during collision with a wall analysed by image processing. Exp Fluids 1993;15:91–6.
[48] Abuku M, Janssen H, Poesen J, Roels S. Impact, absorption and evaporation of raindrops on building facades. Build Environ 2009;44:113–24. doi:10.1016/j.buildenv.2008.02.001.
[49] Roisman IV, Horvat K, Tropea C. Spray impact: rim transverse instability initiating fingering and splash, and description of a secondary spray. Phys Fluids 2006;18:102104.
[50] Moreira ALN, Moita AS, Panao MR. Advances and challenges in explaining fuel spray impingement: How much of single droplet impact research is useful? Prog Energy Combust Sci 2010;36:554–80.
[51] Tropea C, Marengo M. The impact of drops on walls and films. Multiph Sci Technol 1999;11.
[52] Rosin P, Rammler E. The Laws Governing the Fineness of Powdered Coal. J Inst Fuel 1933;31:29–36.

[53] Ashgriz N. Handbook of atomization and sprays: theory and applications. Springer; 2011.
[54] Babinsky E, Sojka PE. Modeling drop size distributions. Prog Energy Combust Sci 2002;28:303–29. doi:10.1016/S0360-1285(02)00004-7.
[55] Alderliesten M. Mean Particle Diameters. Part VII. The Rosin-Rammler Size Distribution: Physical and Mathematical Properties and Relationships to Moment-Ratio Defined Mean Particle Diameters. Part Part Syst Charact 2013;30:244–57.
[56] Khan AR, Richardson JF. The Resistance to Motion of a Solid Sphere in a Fluid. Chem Eng Commun 1987;62:135–50. doi:10.1080/00986448708912056.
[57] Haider A, Levenspiel O. Drag coefficient and terminal velocity of spherical and nonspherical particles. Powder Technol 1989;58:63–70.
[58] Kelbaliyev G, Ceylan K. Development of new empirical equations for estimation of drag coefficient, shape deformation, and rising velocity of gas bubbles or liquid drops. Chem Eng Commun 2007;194:1623–37.
[59] Morsi SA, Alexander AJ. An investigation of particle trajectories in two-phase flow systems. J Fluid Mech 1972;55:193–208.
[60] Shih T-H, Liou WW, Shabbir A, Yang Z, Zhu J. A new k-ϵ eddy viscosity model for high reynolds number turbulent flows. Comput Fluids 1995;24:227–38.
[61] Saneinejad S, Moonen P, Defraeye T, Derome D, Carmeliet J. Coupled CFD, radiation and porous media transport model for evaluating evaporative cooling in an urban environment. J Wind Eng Ind Aerodyn 2012;104:455–63.
[62] Fiala D, Havenith G, Bröde P, Kampmann B, Jendritzky G. UTCI-Fiala multi-node model of human heat transfer and temperature regulation. Int J Biometeorol 2012;56:429–41.
[63] Jendritzky G, de Dear R, Havenith G. UTCI—Why another thermal index? Int J Biometeorol 2012;56:421–8.
[64] Fiala D, Lomas KJ, Stohrer M. A computer model of human thermoregulation for a wide range of environmental conditions: the passive system. J Appl Physiol 1999;87:1957–72.
[65] Fiala D, Lomas KJ, Stohrer M. Computer prediction of human thermoregulatory and temperature responses to a wide range of environmental conditions. Int J Biometeorol 2001;45:143–59.
[66] Bröde P, Fiala D, B\lażejczyk K, Holmér I, Jendritzky G, Kampmann B, et al. Deriving the operational procedure for the Universal Thermal Climate Index (UTCI). Int J Biometeorol 2012;56:481–94.
[67] Handbook A. HVAC Applications (2007). Am Soc Heat Refrig Air Cond Eng Inc Atlanta GA 2007.
[68] Sommerfeld M, Qiu H-H. Experimental studies of spray evaporation in turbulent flow. Int J Heat Fluid Flow 1998;19:10–22.

FIGURES

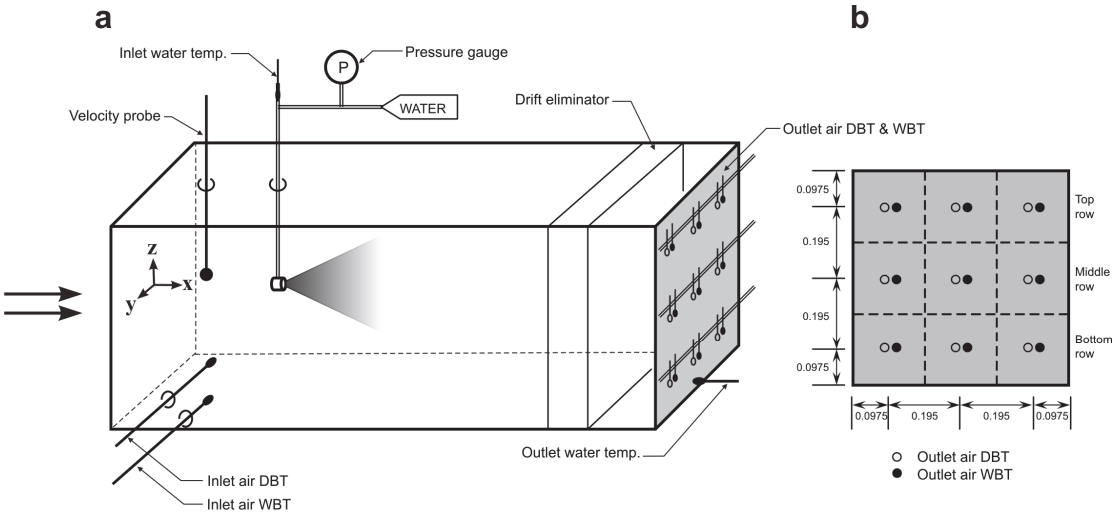

Figure 1. (a,b) Wind-tunnel measurement setup with measurement positions in the outlet plane (modified from [16]). Dimensions in meter.

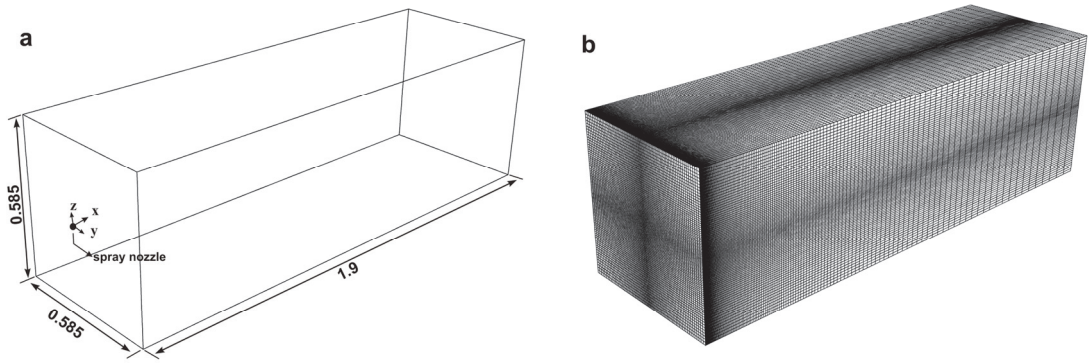

Figure 2. (a) Computational domain (dimensions in meter). (b) Computational grid (1,018,725 cells).

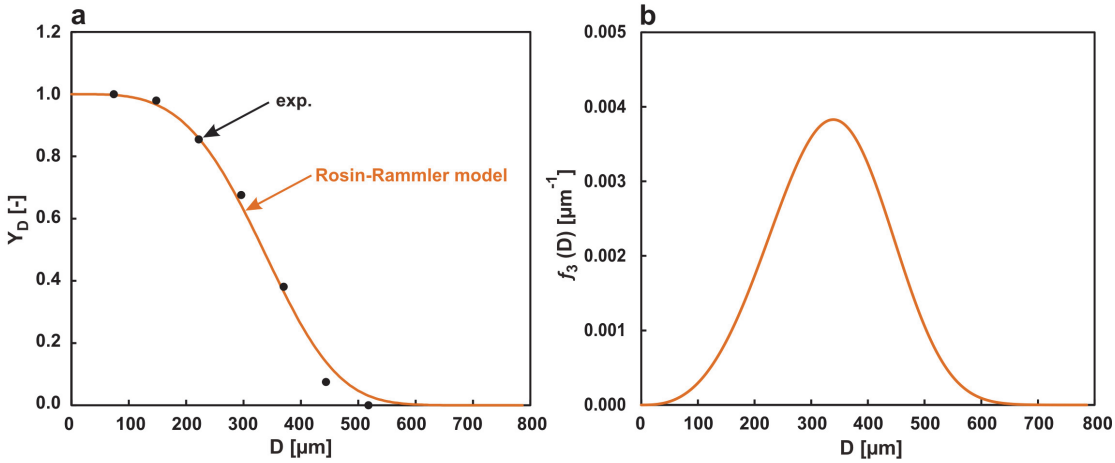

Figure 3. (a) Rosin-Rammler curve fit (solid line) and experimental data of Y_D (dots). (b) Rosin-Rammler volume density distribution.

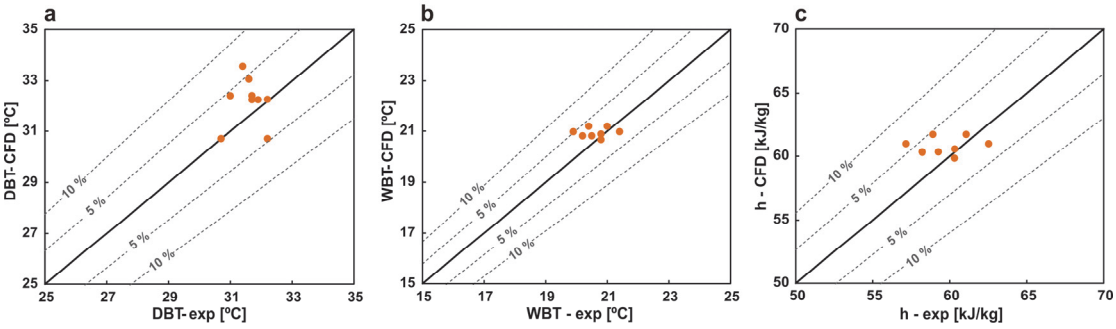

Figure 4. Comparison of calculated (CFD) and measured (exp. [16]) (a) DBT, (b) WBT and (c) specific enthalpy for the reference case.

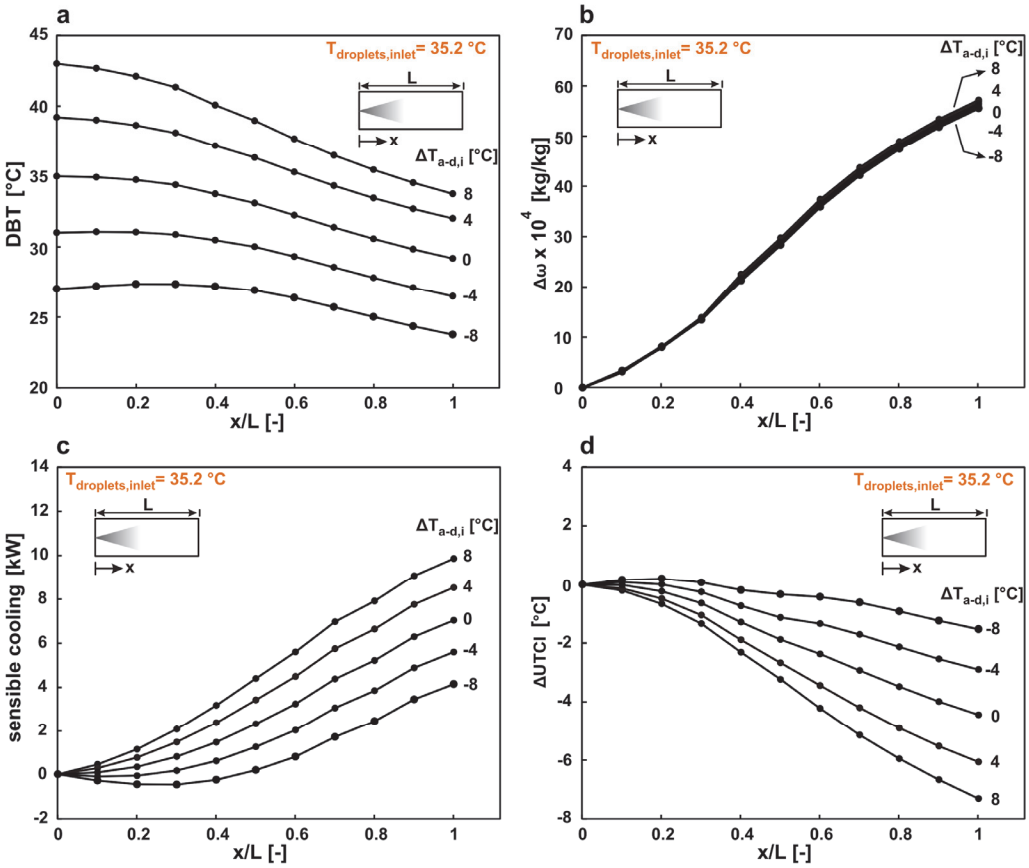

Figure 5. Impact of inlet dry-bulb air temperature: Profiles of (a) average air dry-bulb temperature, (b) humidity ratio variation, (c) sensible cooling and (d) UTCI variation along the domain.

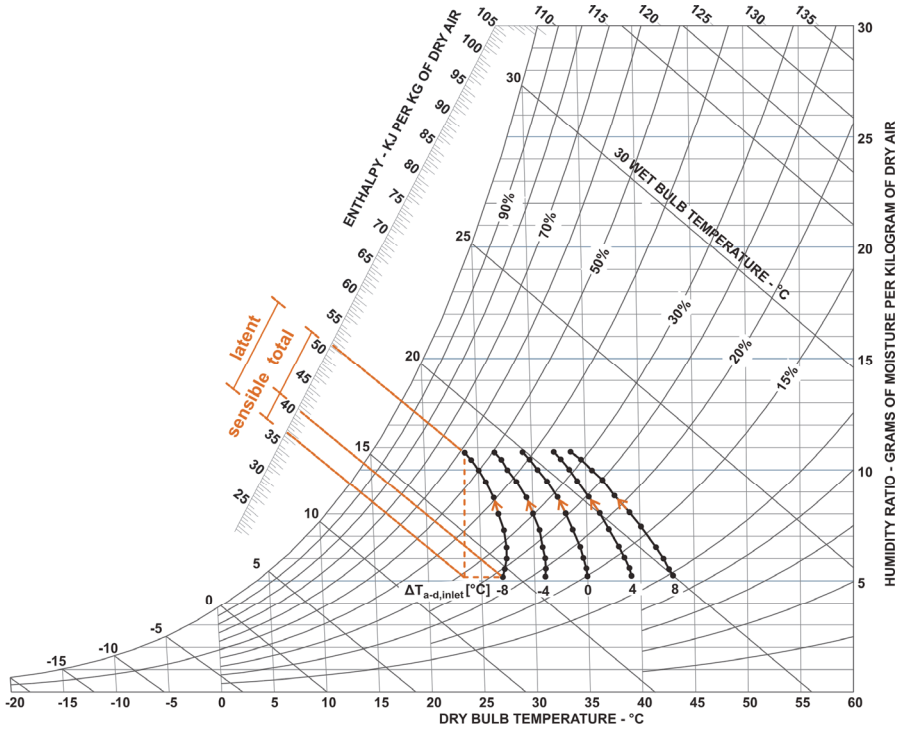

Figure 6. Impact of dry-bulb air temperature: moist air conditions on the psychrometric chart.

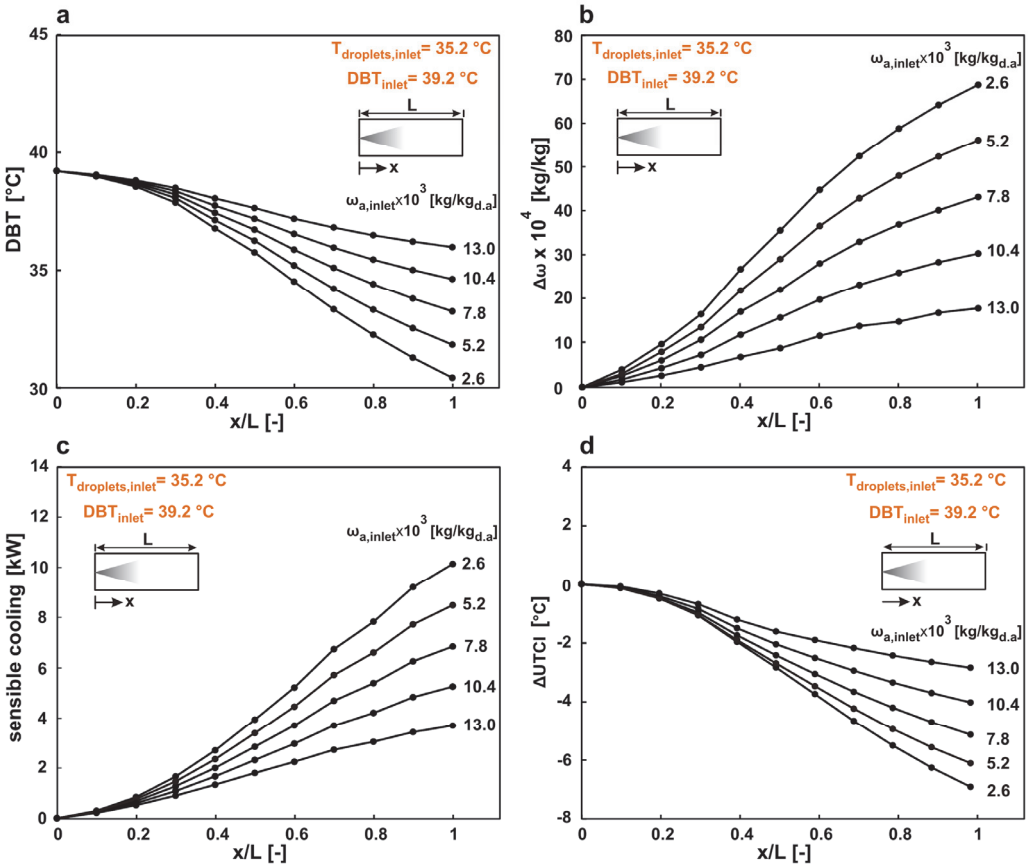

Figure 7. Impact of inlet humidity ratio: profiles of (a) average air dry-bulb temperature, (b) humidity ratio variation, (c) sensible cooling and (d) UTCI variation along the domain.

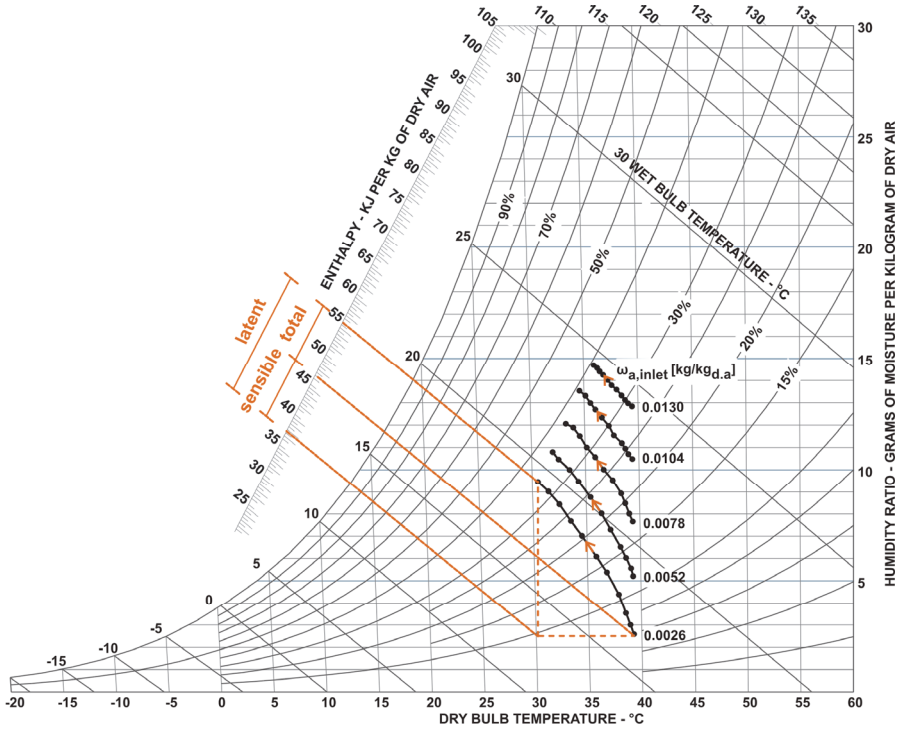

Figure 8. Impact of inlet humidity ratio: moist air conditions on the psychrometric chart.

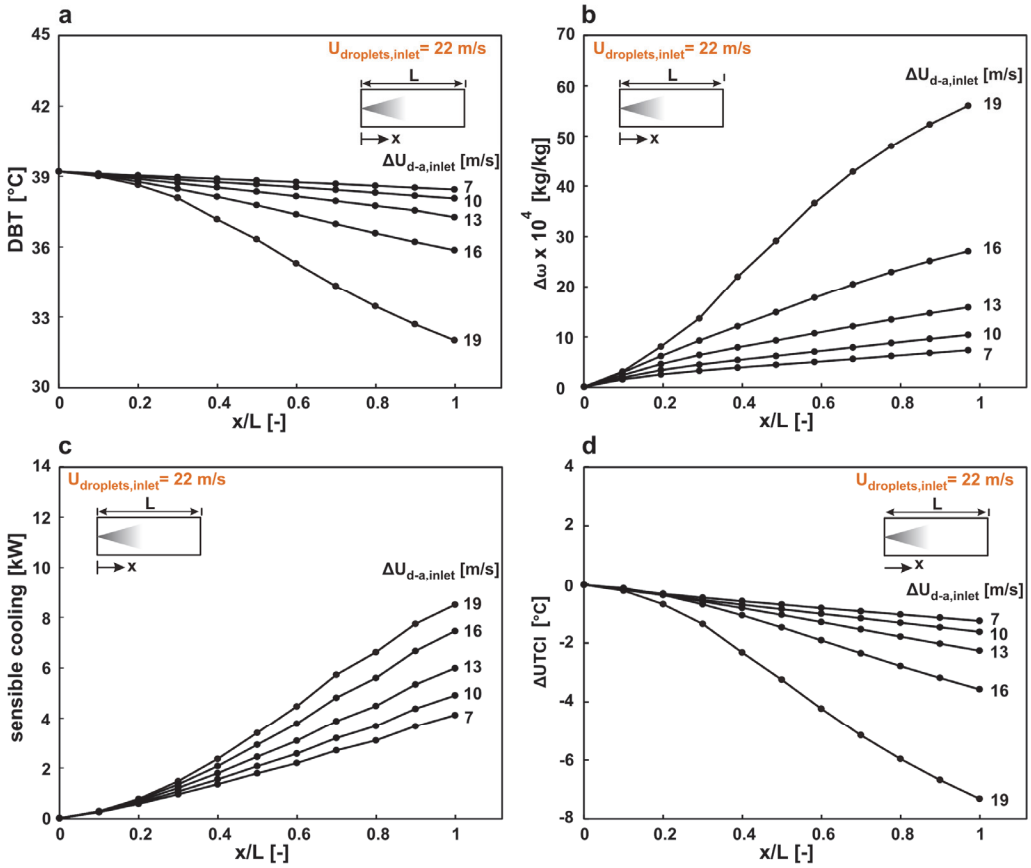

Figure 9. Impact of inlet velocity: profiles of (a) average air dry-bulb temperature, (b) humidity ratio variation, (c) sensible cooling and (d) UTCI variation along the domain.

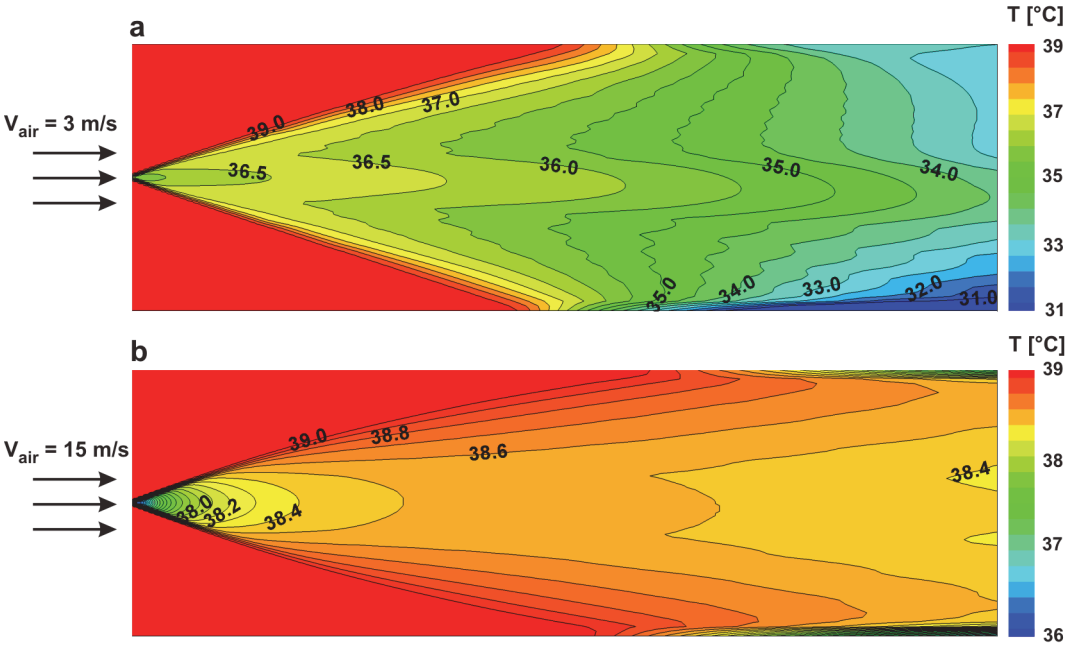

Figure 10. Temperature distribution in cross-section (centre plane) for cases (a) $\Delta U_{d\text{-}a,i}$ = 19 m/s and (b) $\Delta U_{d\text{-}a,i}$ = 7 m/s.

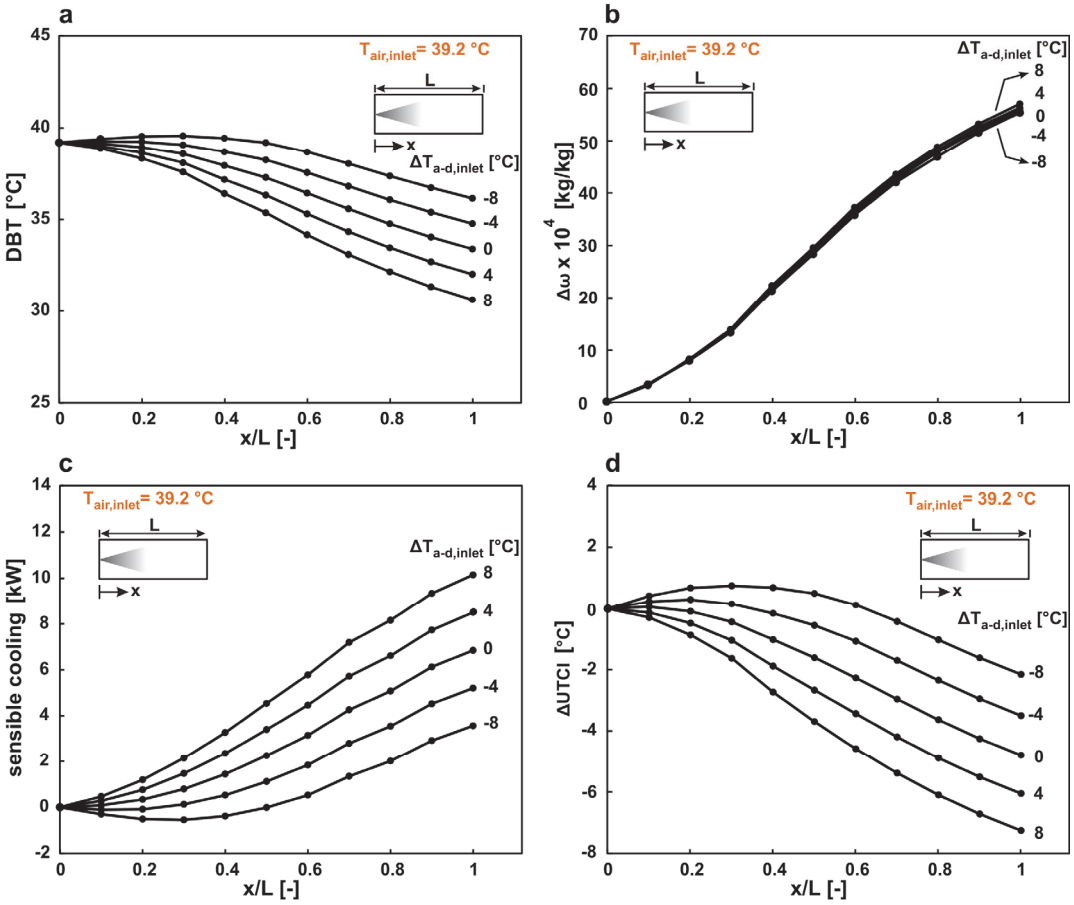

Figure 11. Impact of inlet water temperature: profiles of (a) average air dry-bulb temperature, (b) humidity ratio variation, (c) sensible cooling and (d) UTCI variation along the domain.

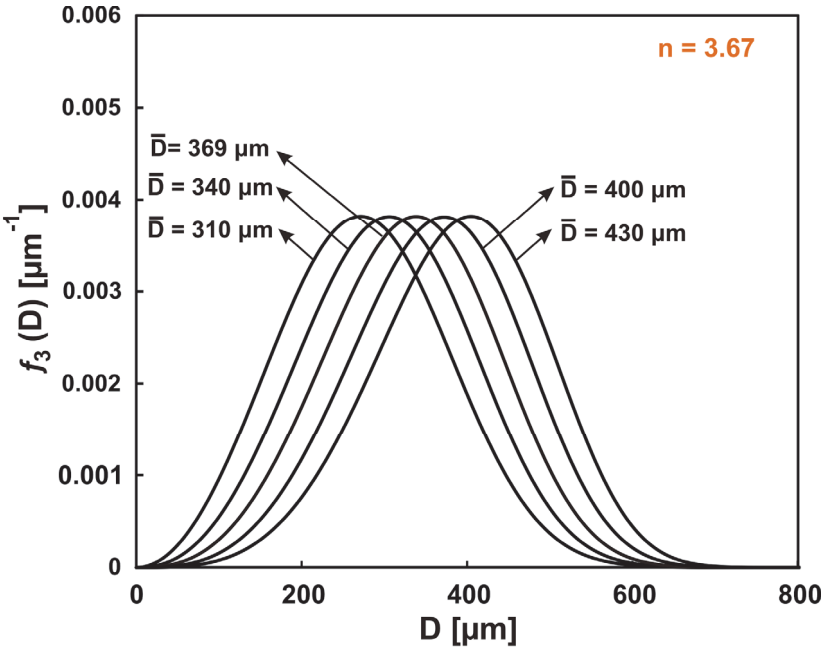

Figure 12. Rosin-Rammler volume density distributions for five values of $\bar{D}$, the mean of distribution.

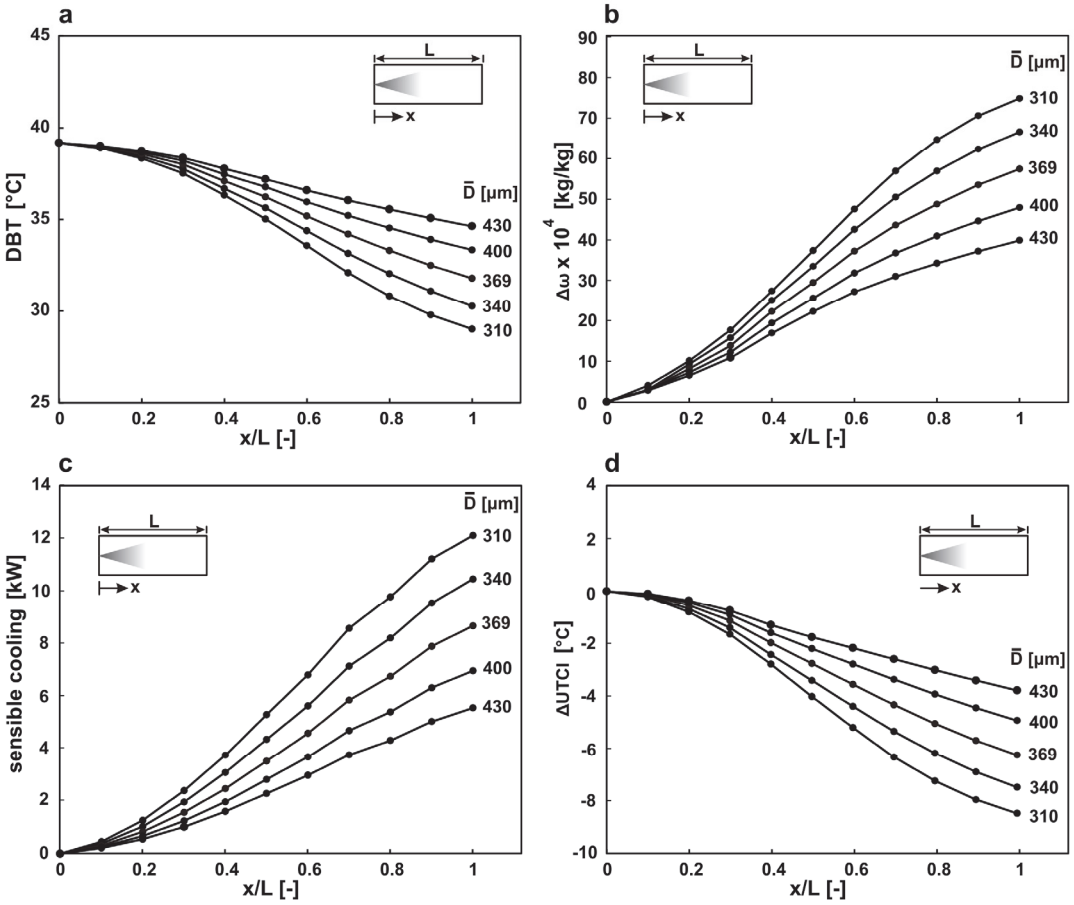

Figure 13. Impact of the mean of the distribution $\bar{D}$: profiles of (a) average air dry-bulb temperature, (b) humidity ratio variation, (c) sensible cooling and (d) UTCI variation along the domain.

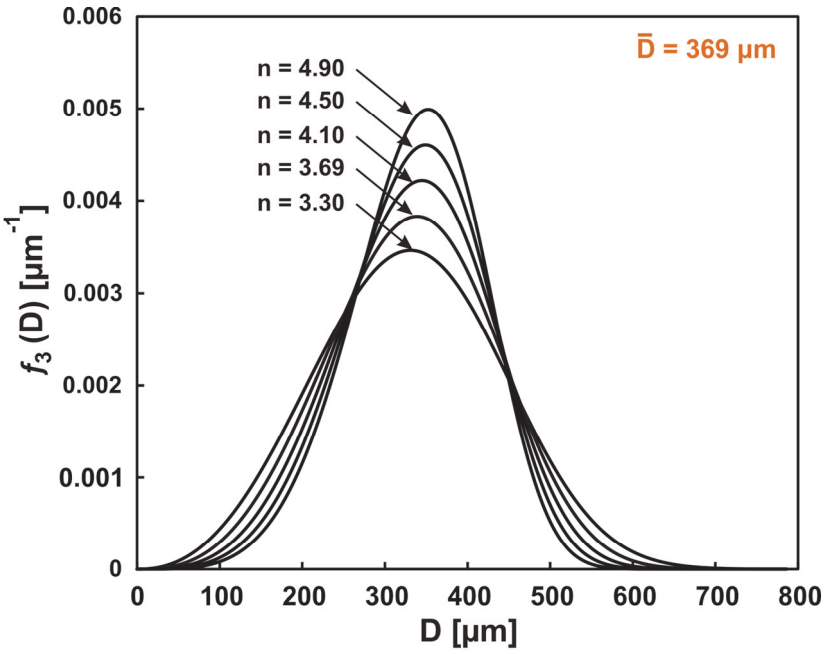

Figure 14. Rosin-Rammler volume density distributions for five values of n, the spread parameter of distribution.

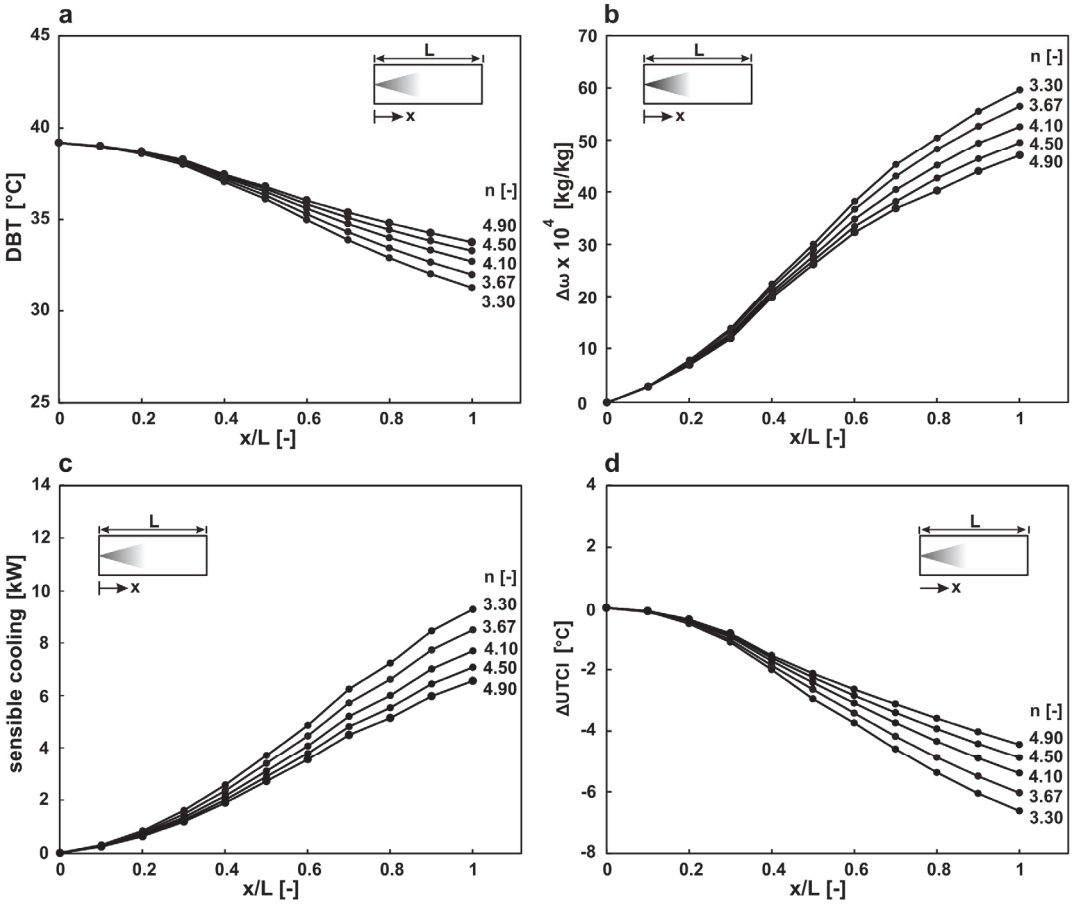

Figure 15. Impact of the spread parameter of distribution, n: profiles of (a) average air dry-bulb temperature, (b) humidity ratio variation, (c) sensible cooling and (d) UTCI variation along the domain.

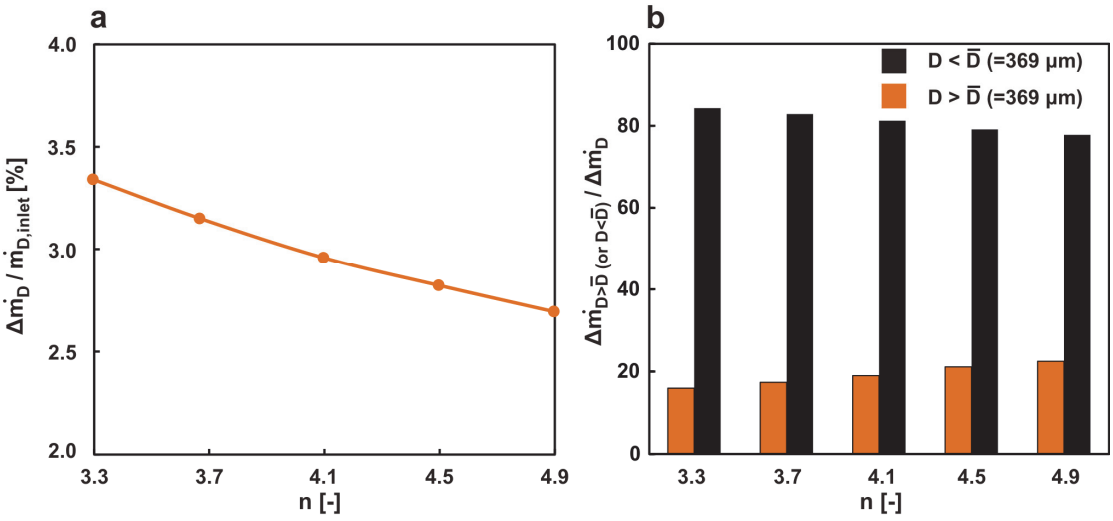

Figure 16. (a) Profile of normalized evaporated droplet mass flow rate for different values of n. (b) Proportion of the evaporated droplets for two droplet size groups: ($D < \bar{D}$) and ($D > \bar{D}$).

TABLES

Table 1. List of some main parameters of the reference case. D is the nozzle discharge diameter and α is the half-cone angle.

Inlet air			Water				Spray nozzle	
V (m/s)	DBT (°C)	WBT (°C)	P (bar)	T_{in} (°C)	T_{out} (°C)	$\dot{m}$ (lit/min)	D (mm)	α (deg.)
3	39.2	18.7	3	35.2	26.1	12.5	4.0	18.0

Table 2. Drag coefficient model constants for different Reynolds numbers.

Re range	K_1	K_2	K_3
Re < 0.1	24.00	0.00	0.00
0.1< Re < 1	22.73	0.09	3.69
1 < Re < 10	29.17	-3.89	1.22
10 < Re < 100	46.50	-116.67	0.62
100 < Re < 1000	98.33	-2778.00	0.36
1000 < Re < 5000	148.62	-47500.00	0.36
5000 < Re < 10000	-490.546	578700.00	0.46
10000 < Re < 50000	-1662.50	5416700.00	0.52

Table 3. List of some main parameters of the cases for the sensitivity analysis.

	Inlet air			Inlet water	Droplet distribution			
	DBT (°C)	ω $kg_{vapour}/kg_{dry\text{-}air}$	V (m/s)	T_{in} (°C)	D_{min} (μm)	D_{max} (μm)	$(\bar{D})$ (μm)	n
Inlet DBT	27.2-43.2	0.0052	3	35.2	74	518	369	3.67
Inlet humidity ratio (ω)	39.2	0.0026 -0.0130	3	35.2	74	518	369	3.67
Inlet air velocity	39.2	0.0052	3-15	35.2	74	518	369	3.67
Inlet water temperature	39.2	0.0052	3	31.2-47.2	74	518	369	3.67
Mean of the distribution $(\bar{D})$	39.2	0.0052	3	35.2	10	800	310-430	3.02-4.00
Spread parameter (n)	39.2	0.0052	3	35.2	10	800	369	3.3-4.9

Table 4. Sensible cooling provided by the system for different values of $\Delta T_{a\text{-}d,inlet}$

$\Delta T_{a\text{-}d,inlet}$	Impact of inlet air DBT (Fig. 5)			Impact of inlet water temperature (Fig. 11)		
	Inlet air DBT (°C)	Inlet water temperature (°C)	Sensible cooling (kW)	Inlet air DBT (°C)	Inlet water temperature (°C)	Sensible cooling (kW)
8	43.2	35.2	9.8	39.2	31.2	10.2
4	39.2	35.2	8.5	39.2	35.2	8.5
0	35.2	35.2	7.1	39.2	39.2	6.8
-4	31.2	35.2	5.6	39.2	43.2	5.2
-8	27.2	35.2	4.1	39.2	47.2	3.6